FARWEST: Efficient Computation of Wave-Particle Interactions for a Dynamic Description of the Electron Radiation Belt Diffusion

Nour Dahmen, Angélica Sicard, Antoine Brunet, Ondrej Santolik, Viviane Pierrard, Edith Botek, Fabien Darrouzet, Christos Katsavrias

Nour Dahmen, Angélica Sicard, Antoine Brunet, Ondrej Santolik, Viviane Pierrard, et al.. FARWEST: Efficient Computation of Wave-Particle Interactions for a Dynamic Description of the Electron Radiation Belt Diffusion. Journal of Geophysical Research Space Physics, 2022, 127 (10), 10.1029/2022JA030518 . hal-03836575

ADVANCING EARTH AND SPACE SCIENCE

JGR Space Physics

RESEARCH ARTICLE
10.1029/2022JA030518

Key Points:

- A new efficient method is proposed to compute wave particle interaction diffusion rates
- The new implementation is numerically accurate and conserve for given inputs, the physical relevance of the computed diffusion rates
- The new method enables a time dependent control of the wave particle diffusion frame by the cold plasma density and VLF intensity dynamics

Correspondence to:
N. Dahmen,
nourallah.dahmen@onera.fr

Citation:
Dahmen, N., Sicard, A., Brunet, A., Santolik, O., Pierrard, V., Botek, E., et al. (2022). FARWEST: Efficient computation of wave-particle interactions for a dynamic description of the electron radiation belt diffusion. *Journal of Geophysical Research: Space Physics*, *127*, e2022JA030518. https://doi.org/10.1029/2022JA030518

Received 1 APR 2022
Accepted 19 SEP 2022

FARWEST: Efficient Computation of Wave-Particle Interactions for a Dynamic Description of the Electron Radiation Belt Diffusion

Nour Dahmen[1], Angélica Sicard[1], Antoine Brunet[1], Ondrej Santolik[2,3], Viviane Pierrard[4], Edith Botek[4], Fabien Darrouzet[4], and Christos Katsavrias[5]

[1]ONERA/DPHY Université de Toulouse, Toulouse, France, [2]Department of Space Physics, Institute of Atmospheric Physics of the Czech Academy of Sciences, Prague, Czechia, [3]Faculty of Mathematics and Physics, Charles University, Prague, Czechia, [4]Royal Belgian Institute for Space Aeronomy BIRA–IASB, Brussels, Belgium, [5]Department of Physics, National and Kapodistrian University of Athens NKUA, Athens, Greece

Abstract In this paper, we present a new method to compute rapidly, wave particle interaction induced pitch angle and momentum diffusion coefficients. Those terms are normally obtained by the numerical solving of equations based on the quasi-linear theory. However, this bulk resolution leads to a high computational cost, preventing the integration of plasma density and VLF waves nowcasts and forecasts. Therefore, and in the context of the SAFESPACE project (H2020), we implemented a new wave particle interaction code called FARWEST (FAst Radiation diffusion with Waves ESTimator), with an efficient interpolation based method. The proposed implementation was validated against reference results obtained by WAPI, ONERA's wave particle interaction legacy code, with a substantial reduction of the computing time while conserving the physical accuracy of the generated coefficients. The FARWEST code is later used to measure the impact of a time-dependent plasma density distribution (numerically computed by BIRA's plasmaspheric model SPM) on the coefficients and on the representation of the electron flux map by Salammbô, ONERA's radiation belt code.

1. Introduction

The balance of seed and loss mechanisms (Lyons & Thorne, 1973) governs electron radiation belt dynamics, while being powered by geomagnetic activity and driven by the solar wind (Hudson et al., 2008). Among these mechanisms, wave particle interactions play a major role. They lead to the violation of the first and the second invariants of the trapped electrons (Schulz & Lanzerotti, 1974), resulting in a pitch angle scattering and momentum transfer (Kennel & Petschek, 1966). During the phases of intense geomagnetic activity, their combined role on particle energization and drain in the atmosphere leads to an electron flux variation over several orders of magnitude within hours (Baker et al., 1986, 1994; Horne et al., 2005; Li et al., 1997).

There are different families of Plasma waves, unevenly distributed in the inner magnetosphere. Besides, each wave type presents different characteristics in terms of induced mechanisms, life time and intensities (Su et al., 2011; Thorne, 2010). On the VLF band, one can cite:

1. Whistler mode Chorus, located outside the plasmasphere, with a frequency range between 10% and 80% of the electron gyrofrequency f_{ce} (Tsurutani & Smith, 1974) (separated into an upper and a lower band). They are responsible for the acceleration and the loss of energetic electrons in the electron outer belt.
2. Plasmaspheric Hiss, trapped inside the plasmasphere with a broadband emission and a frequency range between 100 and 2 kHz. They are responsible for the pitch angle scattering of electrons in the atmosphere which is responsible for the formation of the slot region separating the inner and the outer electron belts (Abel & Thorne, 1998; Lyons et al., 1972).
3. Magnetosonic waves (MS), observed inside and outside the plasmapause, confined within few degrees of the equatorial plane and responsible for accelerations (Horne et al., 2007; Meredith et al., 2008; Thorne, 2010).
4. Electromagnetic Ion Cyclotron (EMIC) waves, observed in the periphery of the plasmasphere and its plume and responsible for sudden losses at relativistic energies due to pitch angle scattering (Meredith, 2003; Summers, 2003; Thorne, 2010; Usanova et al., 2013).

To model these resonant interactions, the quasi-linear theory is used (Kennel & Engelmann, 1966). It yields a diffusion equation that governs the electron distribution and involves pitch angle α and momentum p diffusion

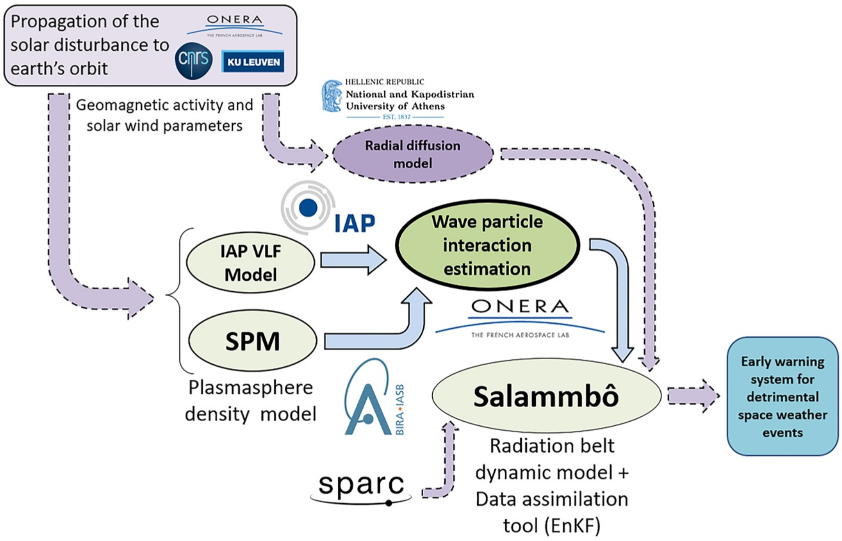

Figure 1. The Wave particle interaction estimation segment inside the SafeSpace project.

coefficients (Albert, 1999; Lyons, 1974a, 1974b). After the emergence of three dimension electron radiation belt codes that required a complete physical description (Beutier & Boscher, 1995; Glauert et al., 2014; Su et al., 2010; Subbotin & Shprits, 2009; Varotsou et al., 2005), different wave particle interaction codes were implemented. They are used to compute bounce averaged diffusion coefficients $\left\langle D_{\alpha_{eq}\alpha_{eq}}\right\rangle, \langle D_{pp}\rangle, \left\langle D_{\alpha_{eq}p}\right\rangle$ (α_{eq} being the equatorial pitch angle) that would serve as input data for the radiation belt dynamic codes.

Starting with particular assumptions to simplify calculations (field aligned propagation, high density assumption) (Albert, 1999; Summers, 2003), the wave particle interaction codes were gradually able to take into account more generalized cases of wave modes, plasma densities and wave propagation angles with the background magnetic field. This was the case of the Pitch Angle and Energy Diffusion of Ions and Electrons code (PADIE) from the British Antarctic Survey (BAS) (Glauert et al., 2014; Glauert & Horne, 2005), ONERA's WAPI code (Sicard-Piet et al., 2008; Sicard-Piet et al., 2014) and ULCA's Full Diffusion Code (FDC) (Shprits et al., 2009). Moreover, they were involved in the analysis of the effect of wave particle interaction parameters such as the cold plasma density on the diffusion rate (Sicard-Piet et al., 2014). In fact, it was shown that the last parameter had a major impact on diffusion rates during active events leading to sudden precipitations of MeV outer belt electrons (Thorne et al., 2005) or accelerations of electrons from keV up to >7 MeV during extreme cold plasma depletion events (Allison et al., 2021).

However, the heavy numerical calculation method used in PADIE, FDC and WAPI (Glauert & Horne, 2005; Ni et al., 2008; Orlova & Shprits, 2011; Shprits et al., 2009; Sicard-Piet et al., 2008) and derived from the analytical quasi-linear theory; imposes a huge computational cost to estimate $\left\langle D_{\alpha_{\mathrm{eq}}\alpha_{\mathrm{eq}}}\right\rangle, \langle D_{pp}\rangle$ and $\left\langle D_{\alpha_{\mathrm{eq}}p}\right\rangle$ (or alternatively $\langle D_{\mathrm{yy}}\rangle$, $\langle D_{\mathrm{EE}}\rangle$ and $\langle D_{yE}\rangle$ with $y = \sin(\alpha_{eq})$) for different geomagnetic activity configurations. For a long time, this computational constraint was not that much bothering as the generation of the different sets of diffusion coefficients could be processed well in advance before the radiation belt simulation runs.

This view has changed since the emergence of the space weather applied field, requiring a time dependent monitoring and reliable predictions of harmful particle populations in the inner magnetosphere. In this sense, the H2020-EU SafeSpace project aims at the implementation of a prototype for a space weather safety service (Daglis et al., 2021). The prototype is built on a chain of physical models, semi-empirical models and statistical tools propagating physical information and uncertainties from the sun to electron radiation belts. Ultimately, the chain will include hourly updated VLF wave information from IAP (Santolík et al., 2021) and cold plasma density distribution, in the plasmasphere and the plasma trough, from BIRA's SPM code (Pierrard et al., 2021; Pierrard & Stegen, 2008; Pierrard & Voiculescu, 2011). This data will then serve as an input to compute each hour, an ensemble of diffusion coefficients that will serve for Salammbô data assimilation simulations (relying on a Ensemble Kalman filter EnKF), as presented in Figure 1 (Daglis et al., 2021).

As the current computational cost of WAPI is inappropriate with the computational requirements of the SafeSpace project that needs the computation of around 200 sets of diffusion coefficients each hour, the ONERA team had to switch to a much more efficient method to compute the latter diffusion coefficients. This constraint led to implementation of a new suitable code called FARWEST (Fast Radiation diffusion with Waves ESTimator), which will be the subject of this paper. In addition to the computational upgrade, the diffusive frame of Salammbô becomes dynamic with FARWEST, as VLF waves and plasma density are updated each time step. This represents a major improvement going in the direction of the previously cited studies, showing the impact of the plasma density dynamic on wave particle interactions.

This paper is organized as follows: Section 2 is devoted to the presentation of the new FARWEST code and its numerical performances. After a quick overview of the old method used in WAPI, we will present the new interpolation based method. Then, in Section 3, we will assess its numerical accuracy compared to WAPI's output and its computational cost. Then, we present in Section 4 the validation procedure operated on FARWEST and measure its physical relevance. In Section 5, we take a further look at the effect of time dependent plasma density inputs on Salammbô's restitution, as the computation of time dependent diffusion coefficients is now enabled with FARWEST. Finally, we conclude our work in Section 6.

2. The FARWEST Code

2.1. The Legacy Implementation of WAPI and Its Performances

In its current version, WAPI computes in the equatorial pitch angle, momentum space (α_{eq},p) the wave-particle interaction diffusion coefficients following the same implementation adopted in BAS's PADIE code (Glauert & Horne, 2005). To do so, a local pitch angle α grid (size $n_\alpha = 100$) is first defined, describing the background magnetic field line traveled by the trapped particles represented by each Salammbô $\left(\alpha_{\mathrm{eq}}, L^*\right)$ grid point. Over this α grid, the corresponding latitudes are computed, allowing to scale the local cold plasma densities N_e and the plasma waves spectrum. In particular, for a given frequency band, a Gaussian power spectral density as a function of the wave frequency ω is assumed

$$B^2(\omega) = \begin{cases} A^2 \exp\left(-\left(\dfrac{\omega - \omega_m}{\delta\omega}\right)^2\right) & \omega_{\mathrm{lc}} \leq \omega \leq \omega_{\mathrm{uc}} \\ 0 & \text{otherwise} \end{cases} \tag{1}$$

with ω_m the frequency of the maximum wave power, $\delta\omega$ the bandwidth, w_{lc}, w_{uc} the lower and upper cutoff frequencies, and A a normalization factor with a linear dependence to the wave amplitude B_ω (see appendix) (Glauert & Horne, 2005). We note that a more generic power spectrum can be obtained by adding several of these Gaussian bands, which is allowed by the linearity of the diffusion coefficients relatively to the power spectrum. In the particular case of WAPI, only Hiss, Lower Chorus and Upper Chorus are considered in the computations (Sicard-Piet et al., 2014). In fact, MS and EMIC are not retained due to their contained spatial extent; limited activity time and energy range (Thorne, 2010) and thus are not considered further in this paper.

Afterward, a Gaussian distribution of wave normal angle $X = \tan(\psi)$ is assumed (ψ is the angle between the $\vec{k}$ the wave vector and earth's magnetic field $\vec{B}$)

$$g(X) = \begin{cases} \exp\left(-\left(\dfrac{X - X_m}{X_\omega}\right)^2\right), & X_{\min} \leq X \leq X_{\max} \\ 0 & \text{otherwise} \end{cases} \tag{2}$$

with X_ω the angular width and X_m the angle for which the distribution is at its maximum. Hence, for each α, the local diffusion coefficients $D_{\alpha\alpha}$, D_{pp}, $D_{\alpha p}$ are given by the following expressions

$$D_{\alpha\alpha} = \sum_{n=n_l}^{n} \int_{X_{\min}}^{X_{\max}} X dX D_{\alpha\alpha}^{nX} \tag{3}$$

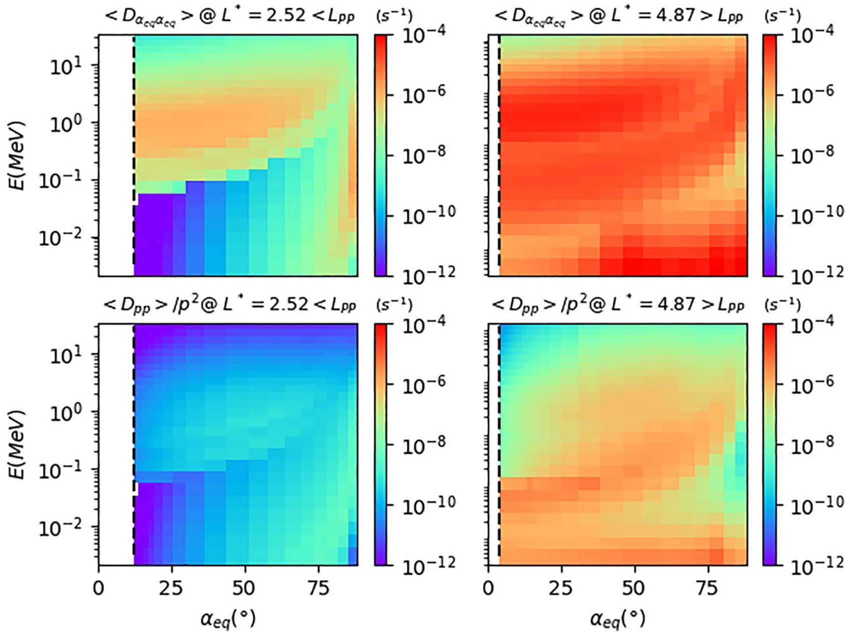

Figure 2. $(\alpha_{\mathrm{eq}}, E)$ distribution of WAPI generated $\langle D_{\alpha_{\mathrm{eq}}\alpha_{\mathrm{eq}}} \rangle$, $\langle D_{\mathrm{pp}} \rangle$ over the Salammbô grid for two L^* on either sides of the plasmapause $(K_p = 2.3)$. The dashed vertical lines represent the loss cone limit.

$$D_{\mathrm{pp}} = \sum_{n=n_l}^{n_h} \int_{X_{\min}}^{X_{\max}} X dX D_{pp}^{nX} \tag{4}$$

$$D_{\alpha\mathrm{p}} = \sum_{n=n_l}^{n_h} \int_{X_{\min}}^{X_{\max}} X dX D_{\alpha p}^{nX} \tag{5}$$

in which local diffusion coefficients for a given harmonic and a given angle $D_{\alpha\alpha}^{nX}$, D_{pp}^{nX}, $D_{\alpha p}^{nX}$ are integrated over all the considered normal angles and summed over the harmonics of the cyclotron frequency (between the lowest and the highest harmonic numbers n_l,n_h). The distributions $B^2(\omega)$ and $g(X)$ are present inside the integrals through the expressions of $D_{\alpha\alpha}^{nX}$, D_{pp}^{nX}, $D_{\alpha p}^{nX}$ (reported in the appendix) (Glauert & Horne, 2005).

Furthermore, the integrations and summations are evaluated at the parallel component of the wave vector $k_\|$ and ω satisfying the resonance equation

$$\omega - k_\| v_\| = \frac{n\Omega_e}{\gamma} \tag{6}$$

and the dispersion equation

$$D(\omega, k, X) = \left(SX^2 + P\right)\mu^4 - \left(\mathrm{RLX}^2 + \mathrm{PS}\left(2 + X^2\right)\right)\mu^2 + \mathrm{PRL}\left(1 + X^2\right) = 0 \tag{7}$$

with $v_\|$ the parallel component of the particle velocity, Ω_e the cyclotron frequency of electrons, R,L,S,P the Stix parameters (Stix, 1962) and $\mu = |c|k/\omega$ the wave reflective index.

Finally, the calculation ends in WAPI with the averaging of local coefficients $D_{\alpha\alpha}$, $D_{\mathrm{pp}}D_{\alpha\mathrm{p}}$ over the bounce motion (Lyons et al., 1972) (see appendix) and over the drift motion. Hence, the obtained averaged coefficients $\langle D_{\alpha_{\mathrm{eq}}\alpha_{\mathrm{eq}}} \rangle$, $\langle D_{\mathrm{pp}} \rangle$, $\langle D_{\alpha_{\mathrm{eq}}p} \rangle$ are suitable to be used in Salammbô 3D simulations (see Figure 2).

In terms of input data, the WAPI considers:

1. Static profiles of B_ω constructed from Dynamics Explorer 1, CRRES, Cluster 1, Double Star TC1, and THEMIS A, D, E satellite measurements (Meredith et al., 2012).

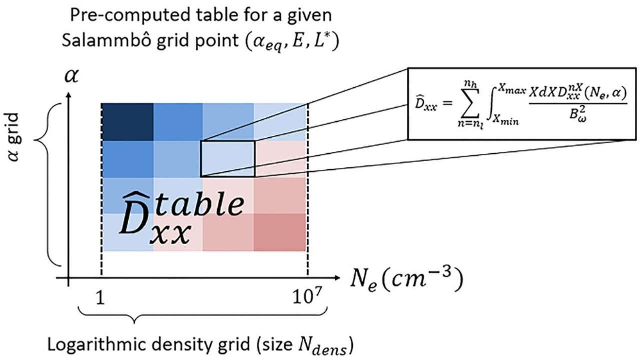

Figure 3. Construction of the B_ω^2 normalized local diffusion coefficient table in step 1 and 2.

2. Semi-empirical (Carpenter & Anderson, 1992) or empirical models for the cold plasma density (Sicard-Piet et al., 2014).

In terms of computational cost, the current version of WAPI takes 3 hr to evaluate one set of the diffusion coefficients $\langle D_{\alpha_{eq}\alpha_{eq}} \rangle \langle D_{pp} \rangle , \langle D_{\alpha_{eq}p} \rangle$, representing one data assimilation member, on a grid with $n_{L^*} \times n_p \times n_{\alpha_{eq}} = 34 \times 25 \times 34$ points.

With its current computational performance, it is obvious that WAPI is not adapted to the SafeSpace project, requiring the computation of ≈200 sets of diffusion coefficients over the Salammbô grid, for each hour of the simulated time. Therefore, it was necessary to develop a new method to compute wave particle interactions while ensuring a much smaller computing time.

2.2. The Computing Logic of FARWEST

For the sake of clarity, we introduce the generic term D_{xx} that refers to any pitch angle or momentum local diffusion coefficient ($D_{\alpha\alpha}$ or D_{pp}) evaluated for a given pitch angle α at a given Salammbô grid point $\left(\alpha_{eq}, p, L^*\right)$.

The new implementation is derived from two observations:

1. The linear dependence of local diffusion coefficients D_{xx} to the squared wave amplitude B_w^2 (Glauert & Horne, 2005) (see appendix).
2. The nonlinear dependence of local diffusion coefficient D_{xx} to the cold plasma density N_e.

Hence, the new adopted strategy is organized in the following order:

1. First, a logarithmic density grid is fixed with a defined size n_{dens}, between the bounds $N_{e_{min}} = 1\,cm^{-3}, N_{e_{max}} = 10^7 cm^{-3}$ (n_{dens} will be set later in this paper).
2. Second, for a given α and a given Salammbô grid point $\left(\alpha_{eq}, p, L^*\right)$, we compute $B_\omega{}^2$ normalized local diffusion coefficients over the newly defined logarithmic density grid, using Equations 3–5 (assuming a normalized wave frequency distribution). This leads to the construction of a normalized diffusion coefficient table that we will refer to as $\hat{D}_{xx}^{table}$ (the$\hat{}$ superscript refers to a B_ω^2 normalized quantity). Thus, for a given Salammbô grid point, we dispose of a 2D (α, N_e) mapping of $\hat{D}_{xx}^{table}$ over the logarithmic density and the local pitch angle grids (see Figure 3).
3. Third, a density model $N_e{}^{model}$ is considered as an entry over $n_{lat} = 4$ magnetic latitude bins, from which we interpolate a density distribution over the α grid, called N_e^{interp}. The four magnetic latitude bins, that will also receive B_ω^2 entries, are parts of the SafeSpace specifications and fixed by SPM's output density format over a $n_{MLT} \times n_{L^*} \times n_{lat}$ grid (see Figure 4).
4. Fourth, the interpolated density N_e^{interp} on a givenα, is used to interpolate from the $\hat{D}_{xx}^{table}$ table, a normalized local diffusion coefficient $\hat{D}_{xx}^{interp}$ (see Figure 4). This interpolation is normally done using a log-log

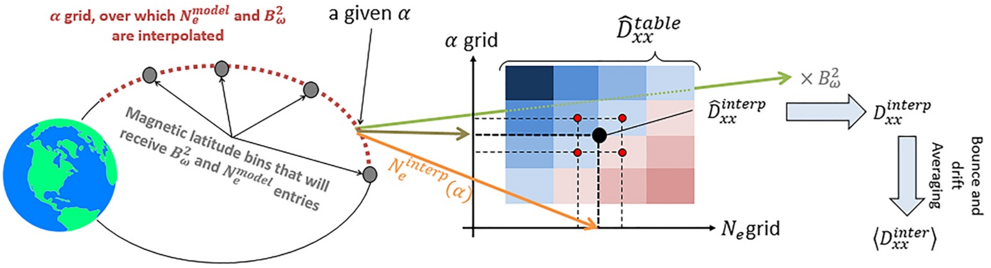

Figure 4. Schematization of steps 3 to 6 for a given α: the α grid (on the left) and the B_ω^2, $N_e{}^{model}$ entries that will serve in the interpolation from the normalized coefficients table (in the center) to the B_ω^2 multiplication and bounce/drift averaging (on the right).

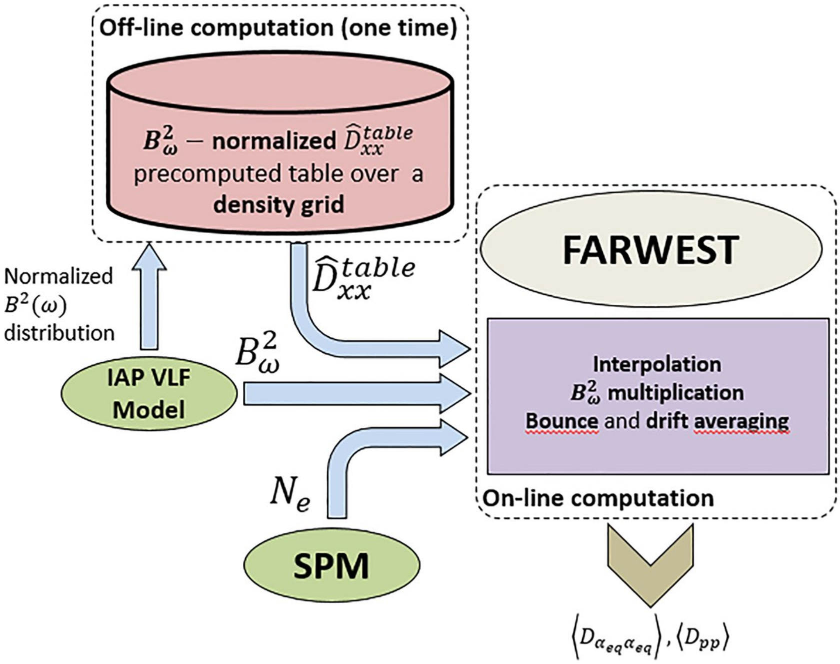

Figure 5. Fast radiation diffusion with waves ESTimator input/output structures inside safespace.

interpolation scheme. For the particular case of an interpolation between a resonant and a non-resonant state, a linear interpolation is used instead, as one of the interpolation bounds is equal to zero.

5. Fifth, the obtained local diffusion coefficient $\hat{D}^{\mathrm{interp}}_{\mathrm{xx}}$ is multiplied by a time-dependent VLF wave intensity B^2_ω to obtain the local diffusion coefficient D^{interp}_{xx} (see Figure 4).
6. Finally, the computed D^{interp}_{xx},for each node of the α grid are averaged over complete drift shells to get the global diffusion coefficients $\left\langle D^{\mathrm{interp}}_{\alpha_{\mathrm{eq}}\alpha_{\mathrm{eq}}} \right\rangle, \left\langle D^{\mathrm{interp}}_{\mathrm{pp}} \right\rangle$ (see Figure 4).

With this method, the computational cost is expected to shrink, as the interpolation operation over the density grid is much less time consuming than the estimation of the expressions 3–5 along with the on-line resolution of the dispersion and resonance equations. In the case of FARWEST, these costly operations are done only once during the construction of the B^2_ω-normalized $\hat{D}^{\mathrm{table}}_{\mathrm{xx}}$ table (see Figure 5). Not to mention the marginal computation cost of the B^2_ω multiplication. As we will see in the following section, the on-line computation time is brought from the order of a few hours to about 1 minute for each set of plasma density and wave intensity entries. Note that in the current version of Salammbô, cross diffusion terms $\left\langle D_{\alpha_{eq}p} \right\rangle$ are ignored for numerical stability considerations (Dahmen et al., 2020; Varotsou et al., 2005). Hence, we will only be interested, in what follows, in the calculation of $\left\langle D_{\alpha_{\mathrm{eq}}\alpha_{\mathrm{eq}}} \right\rangle$ and $\langle D_{\mathrm{pp}} \rangle$.

3. Assessing the Accuracy of FARWEST

The computing method of FARWEST relies on interpolations. This characteristic will surely introduce numerical errors that may affect its numerical accuracy. Therefore, before validating FARWEST, it was important to measure the numerical errors introduced by FARWEST and analyze their origin if possible. We keep in mind that uncertainties are already present in the current modeling of wave particle interaction due for example, to the application range of the quasi-linear theory or the precision of wave distributions and they are not under the scope of this section.

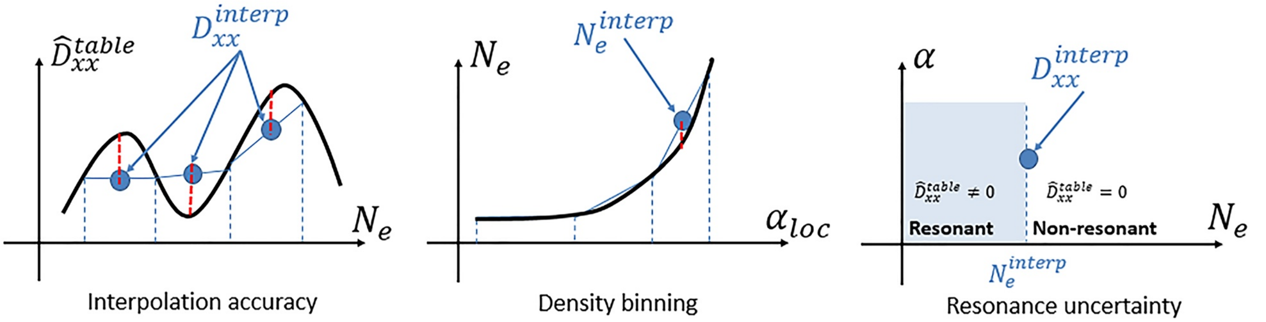

Figure 6. Simplified representation of the three error sources.

We identified three sources of numerical errors (as schematized in Figure 6):

1. Interpolation accuracy. This error is related to the interpolation of the local diffusion coefficients $\hat{D}_{\mathrm{xx}}^{\mathrm{interp}}$ from the $\hat{D}_{\mathrm{xx}}^{\mathrm{table}}$ table and is controlled by the refinement of the density grid (or its size n_{dens}).
2. The constrained density binning. This source of error is not directly linked to the new computing method, but to the relatively coarse representation of the plasma density. It takes origin at the estimation of densities over the α grid based on the interpolation of four magnetic latitude density bins, received from the input density model. This error cannot be controlled as the number of input bins is fixed within the SafeSpace project constraints.
3. Resonance uncertainty. This error is related to the management of special interpolation cases between a resonant $\left(\hat{D}_{\mathrm{xx}}^{\mathrm{table}} \neq 0\right)$ and a non-resonant state $\left(\hat{D}_{\mathrm{xx}}^{\mathrm{table}} = 0\right)$. It is controlled by the refinement of the density grid.

To isolate each one of these errors, we conducted several estimations of local bounce averaged diffusion coefficients, using WAPI and FARWEST and considering the following input data:

4. Three Gaussian profiles for $B(\omega)$ with $\omega_1 = 200\ Hz$, $\delta\omega_1 = 300\ Hz$ and $\omega_2 = 800\ Hz$, $\delta\omega_2 = 500\ Hz$ and $\omega_3 = 2500\ Hz$ and $\delta\omega_3 = 1500\ Hz$. B_ω^2 distributions for the three gaussians are reported in Figure 7.

Plasma density inside the plasmasphere following the arbitrary profile presented in Figure 8 and the Carpenter and Anderson model (Carpenter & Anderson, 1992) outside the plasmasphere.

The choice of this input data is not motivated to obtain the most accurate estimation of the diffusion coefficients by WAPI or FARWEST, but rather benefit from their analytical and realistic features to conduct the following accuracy analysis and later the validation of the new computing method in FARWEST.

3.1. Interpolation Error

To measure the interpolation error, we compare for a given Salammbô grid point $\left(\alpha_{\mathrm{eq}}, p, L^*\right)$:

1. D_{xx}^{interp}, the local diffusion coefficient computed by FARWEST (i.e., the local diffusion coefficient interpolated from a pre-computed table, following step 4 and 5 in Section 2.2).
   and
2. D_{xx}^{theory}, the local diffusion coefficient computed by WAPI (i.e., the local diffusion coefficient obtained from the numerical resolution of the quasi linear theory Equations 3–7).

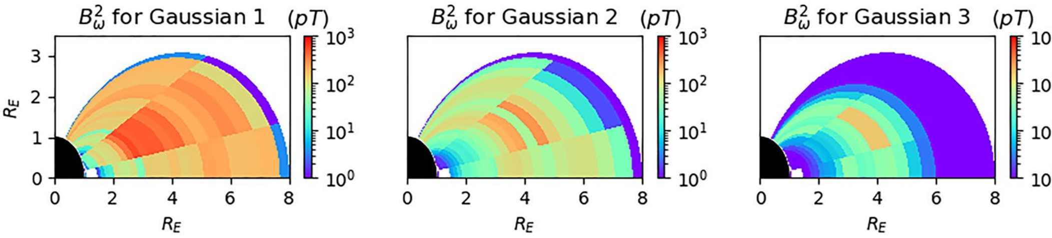

Figure 7. B_ω^2 distributions of each Gaussian as function of Earth's radius and latitude.

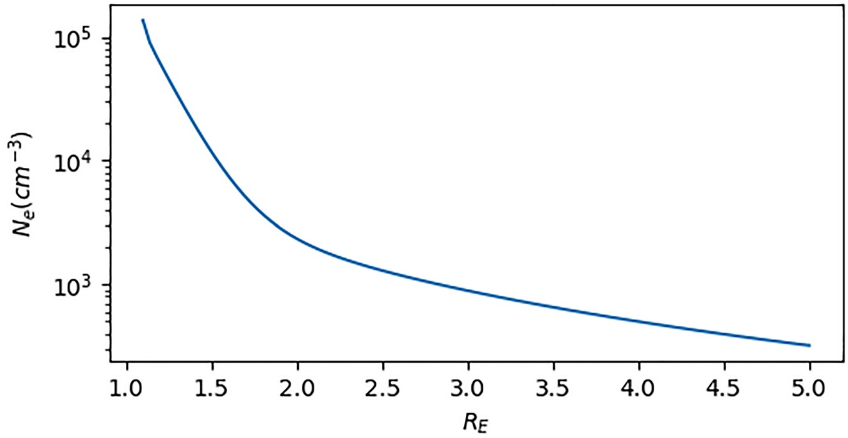

Figure 8. Plasma density model used inside the plasmasphere, as a function of Earth's radius.

To eliminate the density binning error, we consider for WAPI and FARWEST calculations, the same density distribution N_e over the α grid points (in this case, FARWEST is freed from the 4 latitude bin constraint imposed by the SafeSpace project). To compare D_{xx}^{interp} and D_{xx}^{theory} over the α grid, we use the following error expression:

$$Err_\infty = 100 \times \frac{\sup\limits_{\alpha_{loc} \in [0°,90°]} |D_{\text{xx}}^{\text{theory}} - D_{\text{xx}}^{\text{interp}}|}{\sup\limits_{\alpha_{loc} \in [0°,90°]} |D_{\text{xx}}^{\text{theory}}|} \tag{8}$$

We present in Figure 9 the evolution of Err_∞ as a function of the density grid refinement ($n_{\text{dens}} = 25, 50, 75, 100, 150$, and 200 points) for a representative Salammbô grid point.

Obviously, the error decreases as the density grid is refined, begins to stagnate from 100 points. Still, the error magnitudes stay overall lower than 4% for the pitch angle coefficient and lower than 10% for the momentum

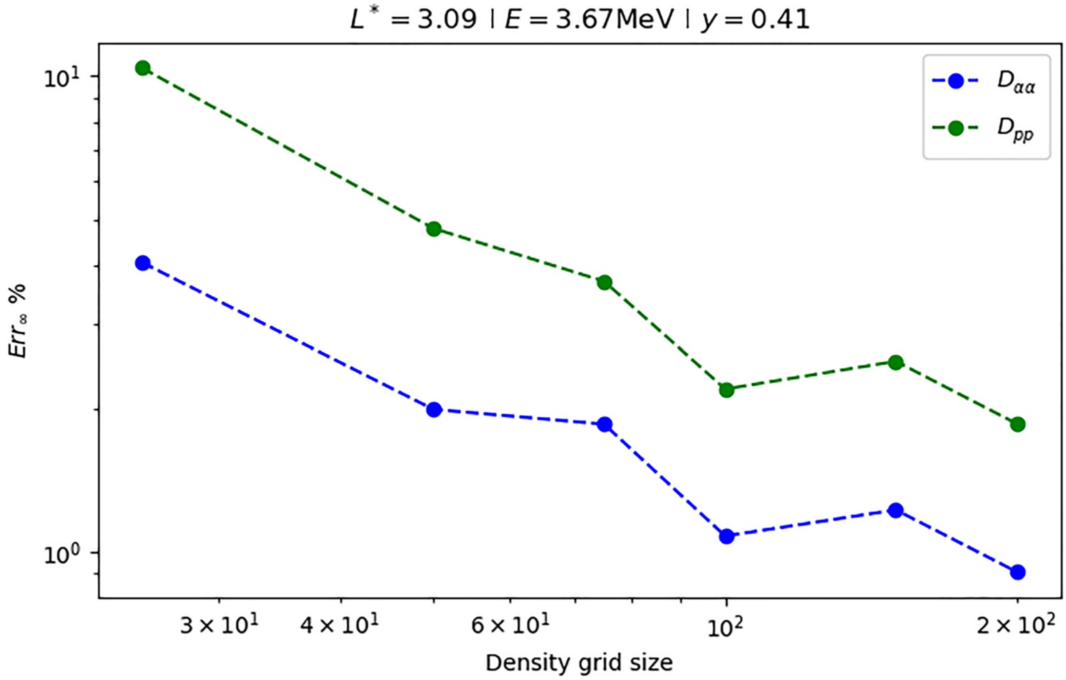

Figure 9. Interpolation error Err_∞ of the local diffusion coefficients $D_{\alpha\alpha}$, D_{pp} evaluated at a representative Salammbô grid point, in case of different density grid refinements.

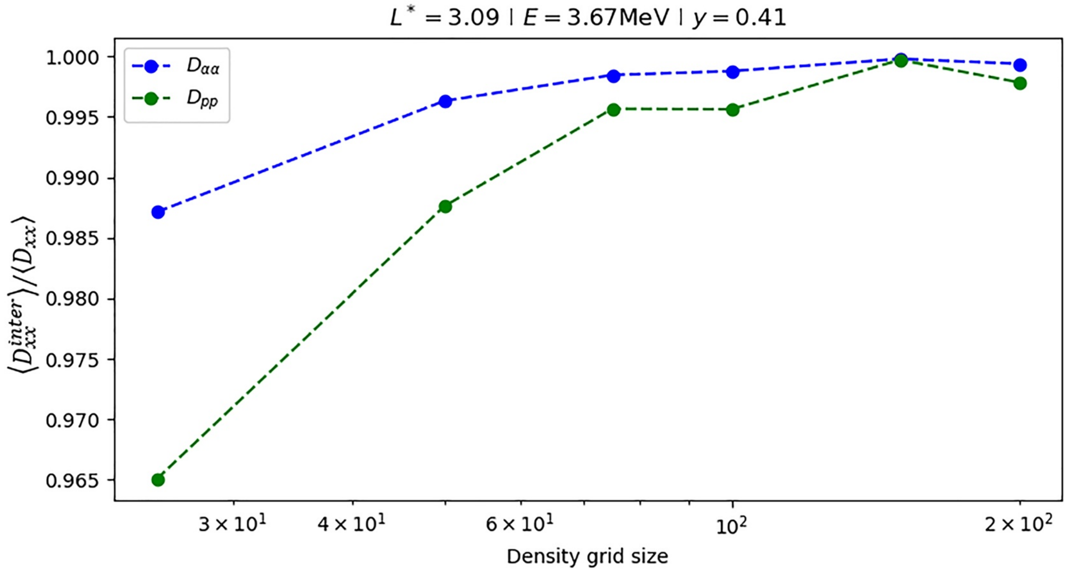

Figure 10. Ratio of analytical and interpolated bounce averaged diffusion coefficients $\left\langle D_{\alpha_{eq}\alpha_{eq}}\right\rangle$, $\left\langle D_{\text{pp}}\right\rangle$ evaluated at a given Salammbô grid point, for different density grid refinements.

coefficient. By construction, Err_∞ focuses on the maximum relative error measured over the local pitch angle grid and we observed that the maximum error is always located near the mirror point ($\alpha = 90°$). This behavior is expected, as the mirror point is the nearest point of the magnetic field line to the atmosphere, where the density is higher and where the logarithmical density grid is less refined, leading to less accurate interpolations.

On the other hand, the ratios of bounce averaged coefficients $\left\langle D_{\alpha_{\text{eq}}\alpha_{\text{eq}}}\right\rangle$, $\langle D_{\text{pp}}\rangle$ presented in Figure 10 reflects lower error magnitudes, even for $n_{\text{dens}} = 25$ points. This is explained by the smoothing effect of bounce averaging that mitigates the effect of local errors over the α grid.

Knowing the huge computational cost required to construct the table $\hat{D}_{\text{xx}}^{\text{table}}$ that has $2 \times n_{L^*} \times n_p \times n_{\alpha_{\text{eq}}} \times n_\alpha \times n_{\text{dens}}$ entries ($\sim O\left(10^6 \times n_{\text{dens}}\right)$), we decided to fix $n_{\text{dens}} = 30$. This will keep the interpolation error to a contained value around 5%–10%. This error margin should still remain lower than the magnitude of the propagated uncertainties along the SafeSpace chain, and originating from its different constitutive physical models.

3.2. Density Binning Error

To measure the density binning error, we need to eliminate both the interpolation and resonance errors from the total error. Thus, we compare bounce averaged coefficients generated by WAPI in case of:

1. A density model N_e^{model} known on each one of the 100 points of the α grid.
2. The same density model known only on the four magnetic latitude bins, that will serve later to estimate N_e^{interp} over the α grid.

Figure 11 shows the ratio of the previously described coefficients (bounce averaged) at locations inside (on the left) and outside the plasmasphere (on the right).

The large majority of Salammbô grid points present a ratio very close to one, especially for $L^* = 4.87$. For $L^* = 2.52$, we observe $\langle D_{\text{pp}}\rangle$ ratios lower than 1 for the points located close to the loss cone at high energy (A) and for points at low energy (C). Besides, some points at low energy and outside the loss cone (B) present null ratios.

To explain the origin of these artifacts we present in Figure 12, a mapping of $\hat{D}_{\text{pp}}^{\text{table}}$ ($n_{\text{dens}} = 30$) as a function of the density N_e and the magnetic latitude orα, for each one of the four group of points identified above (A),(B),(C) and (D). We also represent, on each one of the 2D mappings, the density model followed to compute D_{pp}. The

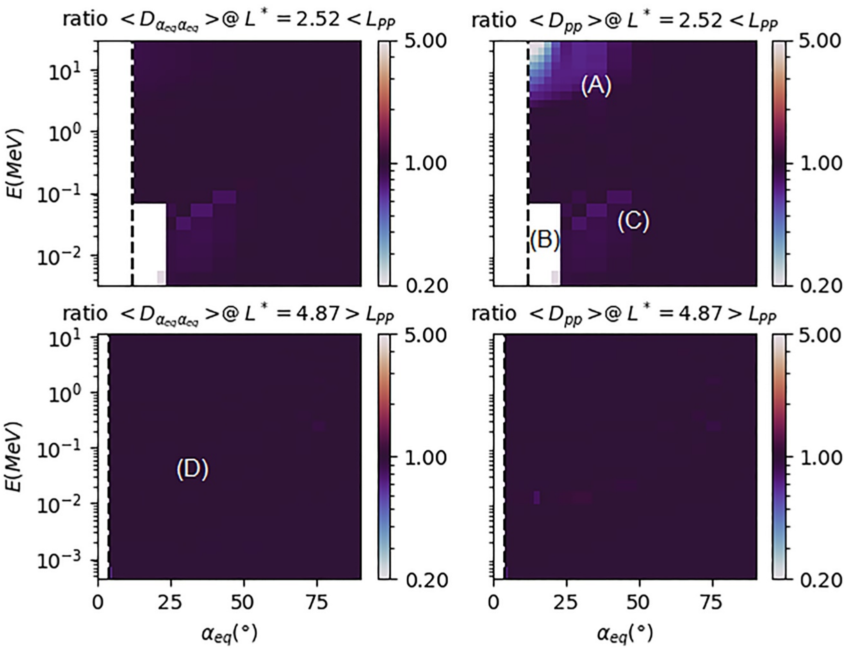

Figure 11. (α_{eq}, E) mappings of ratios measuring the density binning error, on either sides of the plasmapause $(K_p = 2.3)$.

colored areas in the figures represent resonance regions in the (N_e, α) table with $\hat{D}_{\mathrm{xx}}^{\mathrm{table}} \neq 0$, opposed to the white regions where no resonance is observed and $\hat{D}_{\mathrm{xx}}^{\mathrm{table}} = 0$.

For the zone (A), the 60° bin (the highest bin in latitude among the 4 entry bins) is located inside earth $(\frac{R}{R_E} = L^* \sin^2\theta_{60^\circ} = 2.52 \cdot \sin^2(90^\circ - 60^\circ) = 0.63)$. Thus it is outside the density model range (and therefore WAPI's range too) and holds a zero plasma density entry. Consequently, the interpolation misses the local diffusion coefficients of points located between the 40° and 60° bins, leading to an underestimation of the bounce averaged coefficient. For the zone (B), the density model distribution does not encounter any resonant state, leading to a zero interpolated diffusion coefficient. Note that the analytical diffusion coefficient is already very low at that location (see Figure 2). Thus we can expect the interpolation procedure to capture a non zero but very low diffusion coefficient if the density grid is more refined. For zone (C), there are only few resonant states encountered by the density model. Thus, the smoothing effect of bounce averaging is reduced and interpolation errors are emphasized. The opposite behavior is observed with (D) points, for which resonances are observed all along the density distribution path, leading to accurate interpolations and the smoothing of the error during the bounce averaging phase.

3.3. Resonance Uncertainty Error

Isolating the resonance uncertainty error is a difficult task as it is a byproduct of the interpolation operation. In most cases, non-resonant states are observed over continuous regions in the (N_e, α) space and will at most concern few points over the 100 points of the α grid. However, for some cases, the plasma density distribution observed by the particle during its bounce motion can oscillate frequently between non-resonant and resonant states, enhancing the resonance uncertainty error.

This is the case of the (α_{eq}, p, L^*) grid point reported in Figure 13, for which the density model distribution evolve at the frontier separating resonant (in color) and non-resonant (in white) regions. One can have $D_{xx}^{\mathrm{interp}} \neq 0$ (from the linear interpolation between a non-null $\hat{D}_{\mathrm{xx}}^{\mathrm{table}}$and a null $\hat{D}_{\mathrm{xx}}^{\mathrm{table}}$) whereas the WAPI computation gives $D_{xx}^{\mathrm{theory}} = 0$, leading to an overestimation of the coefficient by FARWEST (as we will see later).

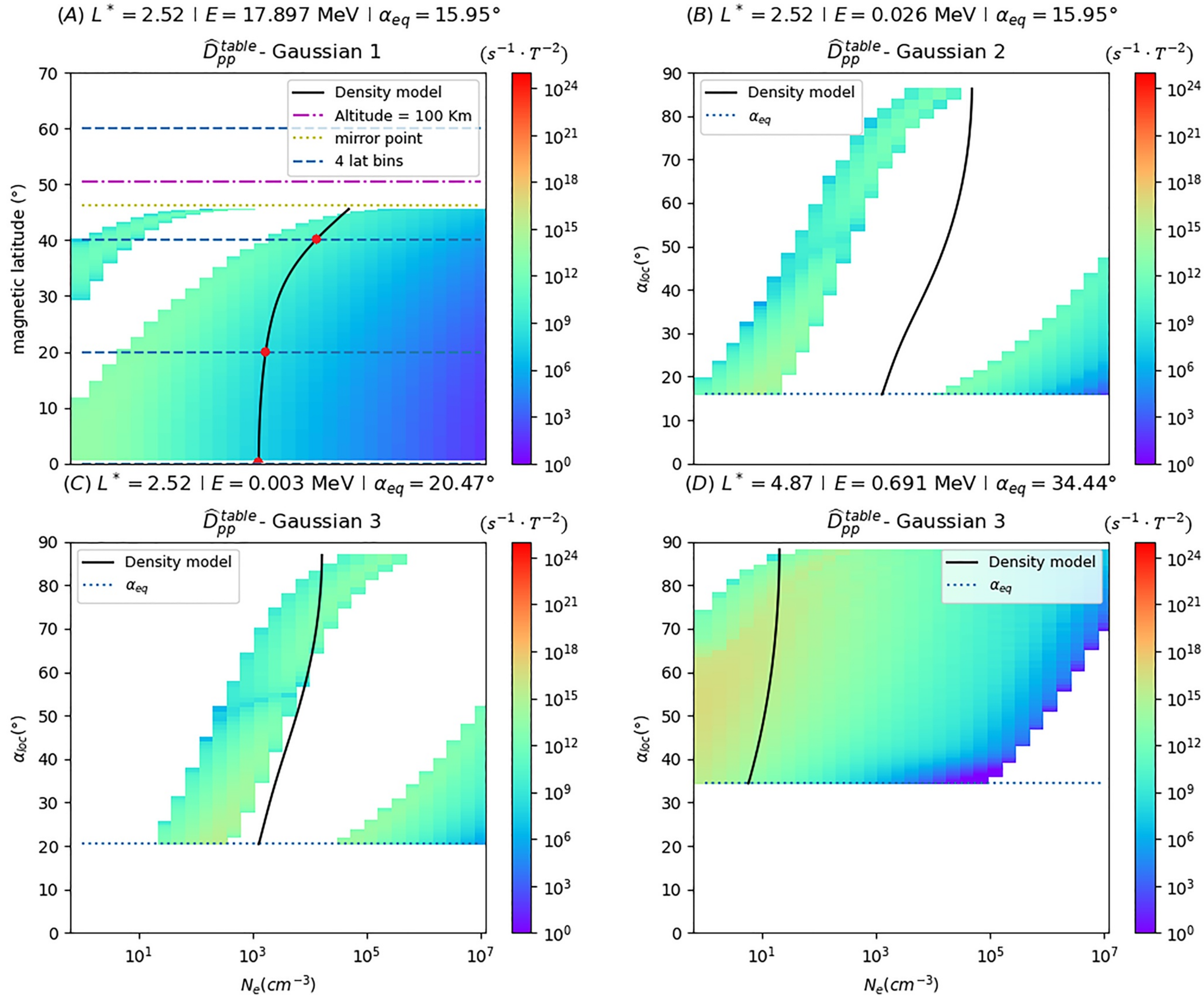

Figure 12. $(N_e, \alpha)\,/\,(N_e, \lambda_m)$ mapping of $\hat{D}_{\rm pp}^{\rm table}(n_{\rm dens} = 30)$ and evolution of the density model for the different (a),(b),(c) and (d) group points and different Gaussians.

4. Validation of the New Code

The validation of FARWEST is based on a two-step procedure:

1. Quantitative comparison of FARWEST and WAPI outputs, using the previously presented density and B_ω inputs (see Figure 14).
2. Qualitative comparison of the diffusion coefficients by measuring their effect on Salammbô simulations (see Figure 16).

4.1. Quantitative Validation

We report in Figure 14, 2*D* mappings of $\left\langle D_{\alpha_{\rm eq}\alpha_{\rm eq}} \right\rangle$ and $\langle D_{\rm pp} \rangle$ generated by WAPI and FARWEST on two L^* plans (inside the plasmasphere at $L^* = 2.52$ and outside the plasmasphere at $L^* = 4.87$). Both codes produce coefficients with practically the same main features and amplitudes. This time, the ratio profiles gathers all three types of errors and one can recognize the (A),(B), and (C) zones identified in the density ratios (Figures 11 and 1). Nevertheless, the majority of ratio values are very close to 1. On the other hand, we report the presence of some overshoots (ratio >1) near $E = 100\ keV$ at $L^* = 2.52$ (E) and $E = 10\ keV$ at $L^* = 4.87$ (F).

Those overshoots are due to the resonance uncertainty error as explained in Section 3c) and showed in Figure 15. In fact, the third Gaussian panel reports several cases of conflicts between D_{xx}^{interp} and D_{xx}^{theory} due to the density model evolving at the edge of the resonant and the non-resonant states. Moreover, the non-zero $\hat{D}_{\mathrm{pp}}^{\mathrm{table}}$ portion crossed by the density distribution is relatively small (compared to the size of the α grid) for the first and the second Gaussians. Thus, the bounce averaging is not efficient enough to smooth the overestimation.

Despite the non-negligible differences observed on the coefficients (especially D_{pp}) in the (A), (B), (E) and (F) zones, their influence over FARWEST's physical relevance and by extension on Salammbô should remain insignificant. In fact, (A), (B), (E) are located inside the plasmasphere where Hiss induced $\left\langle D_{\alpha_{\mathrm{eq}}\alpha_{\mathrm{eq}}} \right\rangle$ and the radial diffusion $D_{L^*L^*}$ highly dominate $\langle D_{\mathrm{pp}} \rangle$. In addition, (B), (E), (F) are located at energies $\leq 100\ keV$, below the confidence range of WAPI. Therefore, those artifacts should not have a notable impact over the physical relevance of FARWEST output.

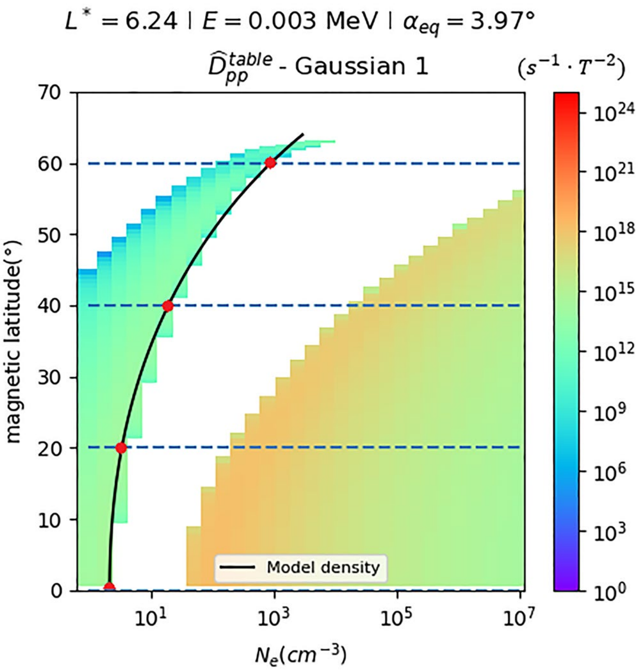

Figure 13. Example of a Salammbô grid point encountering many cases of resonance uncertainty.

4.2. Qualitative Validation

To confirm the previous conclusions, we conducted Salammbô simulations of the St Patrick 2015 CME driven storm, using WAPI and FARWEST generated coefficients and the radial diffusion model taken from (Boscher et al., 2018). The results shown in Figures 16 and 17 present electron flux profiles both nearly coinciding in terms of amplitudes but also in terms of dynamical features as regards to local accelerations (operating at the calm phase at the beginning of the simulation), losses (occurring during the return to the equilibrium phase at the end of the simulations) and the depth of the radial penetration. As expected, the reported artifacts in 4.1 have very small effects at the studied energies. Therefore, we can assert that the new method reconstructs with a very good accuracy the wave particle interaction diffusion coefficients.

4.3. Computational Cost

We report in Table 1, the computational cost of each task in FARWEST (as schematized in Figure 5), evaluated on 8 × 3.5 GHz machine (Intel® Xeon(R) CPU E5-1620 v3) with 8 GB RAM. Compared to WAPI's computation cost, the computational gain of the new code is substantial. In fact, the computing time required to estimate one set of diffusion coefficients over the Salammbô grid was reduced from several hours with WAPI to almost 1 minute with FARWEST. Note that, the computation of one pre-computed table set for 1 Gaussian among 3 (as described in step 2 in 2.2) lasted around 15 hr (but realized once and for all).

Nevertheless, considering the data assimilation application planned within the SafeSpace chain and operating downstream of FARWEST (see Figure 1), a parallel implementation will be required in order to compute the 200 sets of diffusion coefficients. (A serial implementation would still last more than the real time with 1 min × 200 members at each hourly update).

5. Effect of a Time Dependent Plasma Density on Salammbô Simulations: The September 2017 Storm

In this section, we take advantage of FARWEST in order to measure the effect of a time dependent plasma density (computed by BIRA's plasma density code SPM) on Salammbô simulations. The impact of the new VLF waves will be studied in future research works.

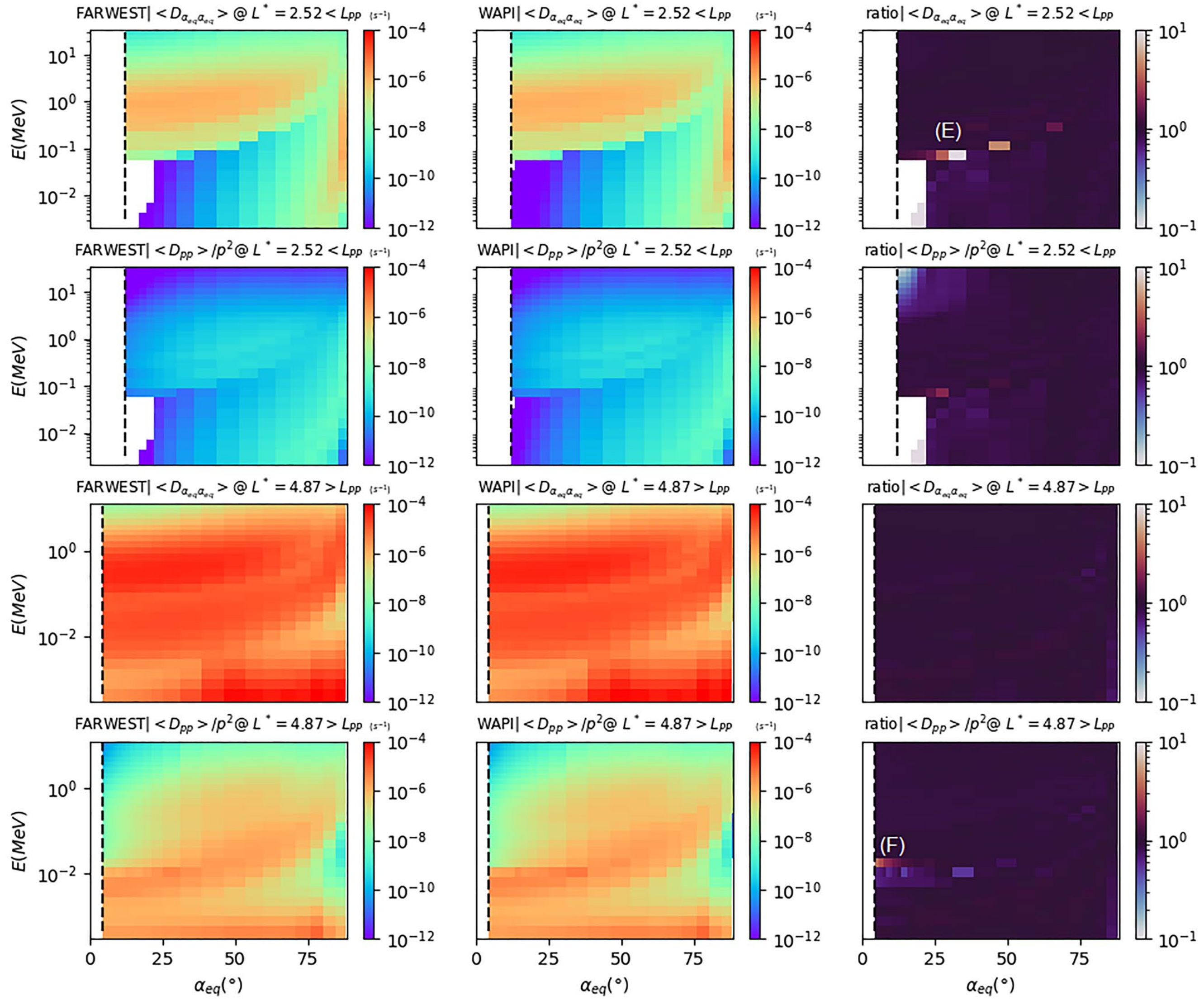

Figure 14. From the top to the bottom, (α_{eq}, E) mapping of $\langle D_{\alpha_{\text{eq}}\alpha_{\text{eq}}}\rangle$, $\langle D_{\text{pp}}\rangle/p^2$ computed byFAst Radiation diffusion with Waves ESTimator, WAPI and their ratios, over Salammbô solving domain at either sides of the plasmasphere $(K_p = 2.3)$.

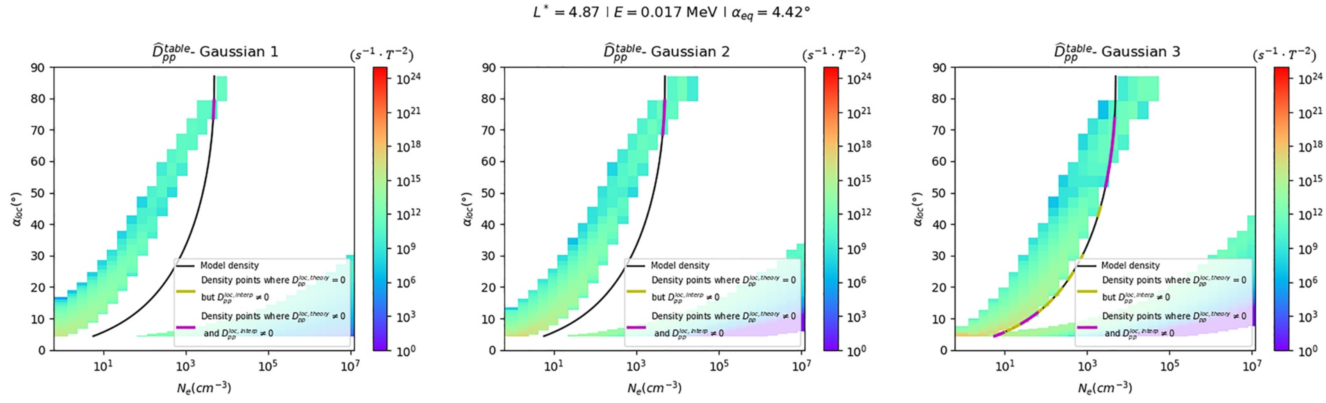

Figure 15. Resonance error example.

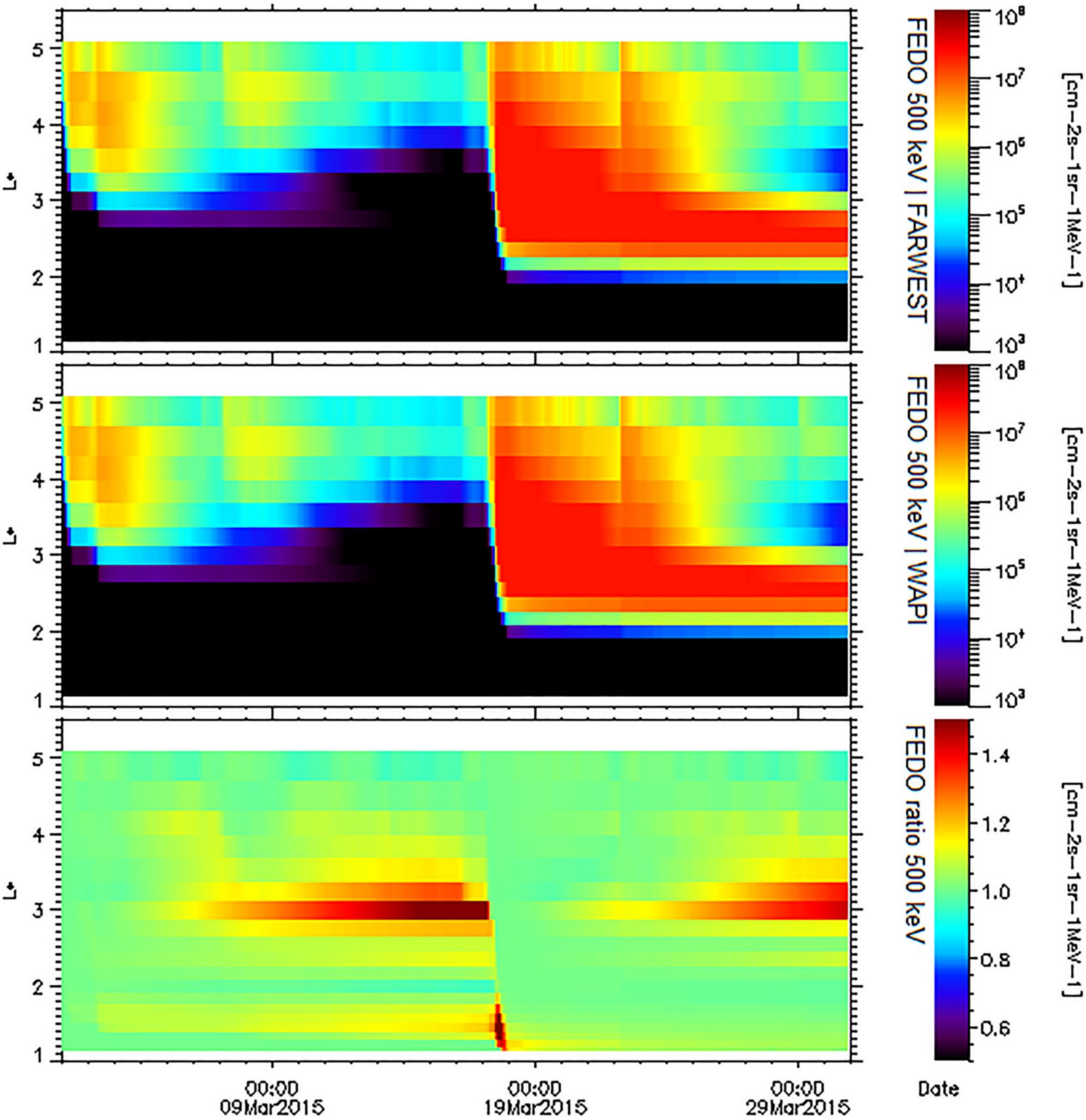

Figure 16. From the top to the bottom: Salammbô 500 keV electron flux for the Saint Patrick event using WAPI generated $\left\langle D_{\alpha_{eq}\alpha_{eq}} \right\rangle$, $\left\langle D_{pp} \right\rangle$, Salammbô 500 keV electron flux using FAst Radiation diffusion with Waves ESTimator generated $\left\langle D_{\alpha_{eq}\alpha_{eq}} \right\rangle$, $\left\langle D_{pp} \right\rangle$ and the flux ratio.

To do so, we conducted two Salammbô simulations of the CME'driven September 2017 event ($T_{\text{simu}} = 23$ days) associated to FARWEST generated $\left\langle D_{\alpha_{eq}\alpha_{eq}} \right\rangle$ and $\langle D_{pp} \rangle$ using the Carpenter and Anderson plasma density model in the first case and using SPM simulated plasma density over the simulation period for the second case. Both simulations use the same radial diffusion model taken from (Boscher et al., 2018) and the same boundary condition at $L^* = 8$, based on averaged THEMIS data (Boscher et al., 2018). We present in Figure 18, the ratio of SPM diffusion coefficients over old WAPI diffusion coefficients (represented in Figure 2) at different L^* plans, over the Salammbô grid. Figures 19 and 20 report the simulation results.

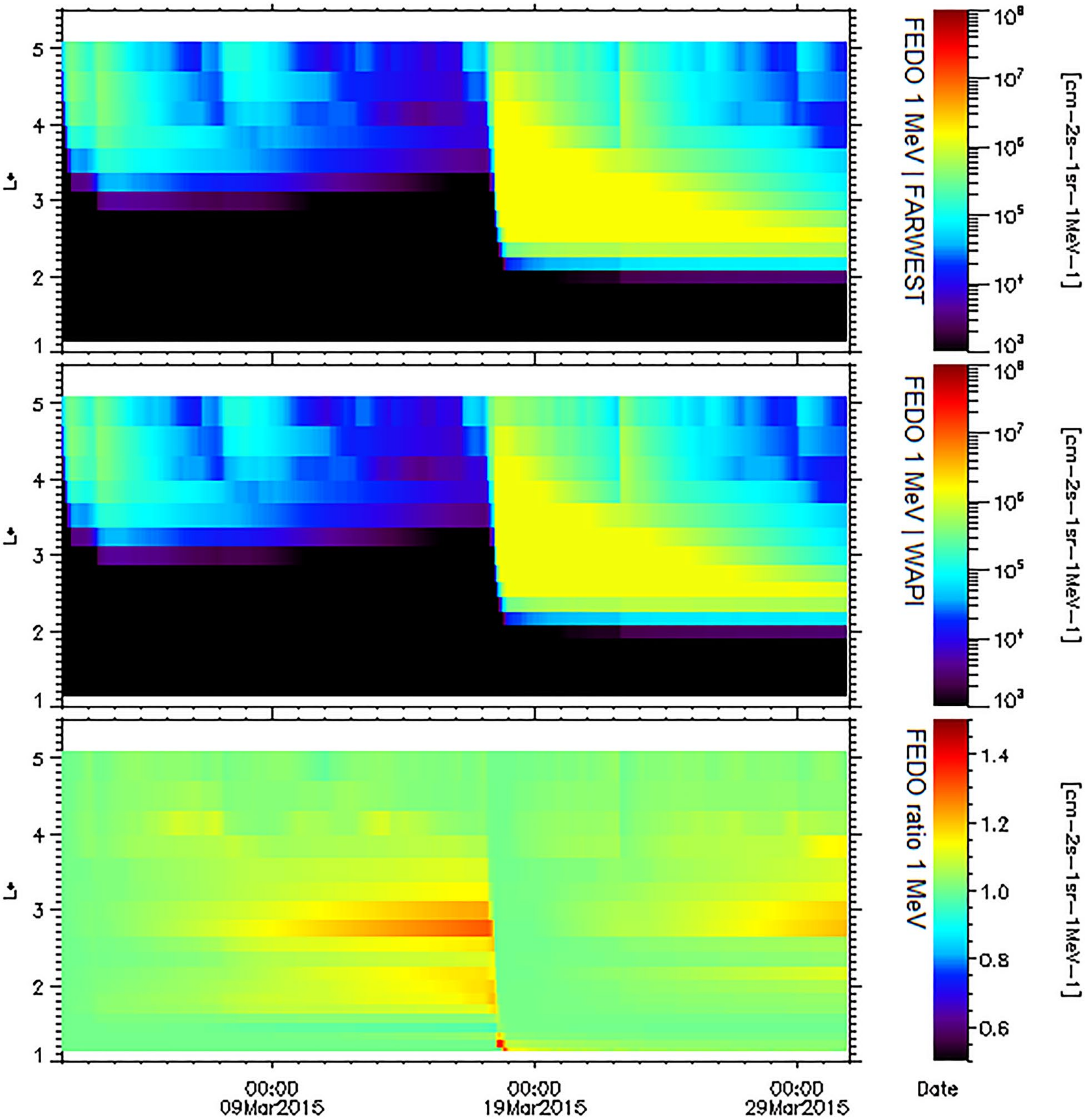

Figure 17. From the top to the bottom: Salammbô 1 MeV electron flux for the Saint Patrick event using WAPI generated $\langle D_{\alpha_{eq}\alpha_{eq}} \rangle$, $\langle D_{pp} \rangle$, Salammbô 1 MeV electron flux using FAst Radiation diffusion with Waves ESTimator generated $\langle D_{\alpha_{eq}\alpha_{eq}} \rangle$, $\langle D_{pp} \rangle$ and the flux ratio.

At 500 keV, both electron profiles are in a good accordance with the measurements in terms of orders of magnitude and dependence to Kp. During the calm period at the early days of September, the SPM density driven simulation presents slightly smaller amplitudes of fluxes around $L^* = 4$ compared to Carpenter density driven simulations and measurements. This is explained by the new local diffusion balance imposed by the new coefficients that slightly favors $\langle D_{\alpha_{eq}\alpha_{eq}} \rangle$ and by extension losses. The increase of pitch angle scattering explains also the small reduction of electron flux magnitude during the main phase of the storm (8–9 September), while still being dominated by radial diffusion. The same behavior is observed during the

Table 1

Computational Cost of FAst Radiation Diffusion With Waves ESTimator (FARWEST) Calculation for One Member and for a Time Updated State

Task	Computing time (s)
B_ω^2 distribution	1.35
N_e distribution	1.03
$D_{\alpha\alpha}$, D_{pp} interpolation	57
B_ω^2 multiplying + bounce and drift averaging	1.35
FARWEST (total)	59.73

return to equilibrium phase at the end of the simulation. This time, the reduction of the estimated flux by the SPM simulation contributes to a better depiction of the slot region. We also observe that the SPM simulation captures better the outer belt's radial depth and its narrowing between September 1st and September 7th, following mechanically the evolution of the plasmapause. This is due to the closer MLT dependence of the SPM density that smooths the state transition between the plasmasphere and the plasma trough.

At 1,000 keV however, both simulations are less accurate and underestimate the measured electron flux. Both simulations show very similar features and dependence to Kp as they embody the same physical balance between radial diffusion and wave particle interaction at that energy. Still, the SPM simulation shows slightly higher flux amplitudes during the early calm period and the return to equilibrium period.

6. Conclusion

In this paper, we presented a new method to compute efficiently wave particle interaction diffusion coefficients. The need for the new method came from the SafeSpace project, aiming at the implementation of a Space weather safety prototype. In particular, the project required the fast computation - for Salammbô EnKF - of an ensemble of pitch angle and momentum diffusion coefficients, each hour, based on cold plasma density and VLF wave entries from upstream codes in the project chain. These requirements were inconsistent with the heavy computational cost imposed by WAPI and other wave particle interaction estimation codes. As a result, a new method was set, which main idea was to pre-compute in one time as much information as possible. The latter came in the form of a density dependent local diffusion coefficients, normalized to VLF waves data. Then, operational diffusion coefficients are interpolated each time, based on plasma density and VLF entries. The new method proved

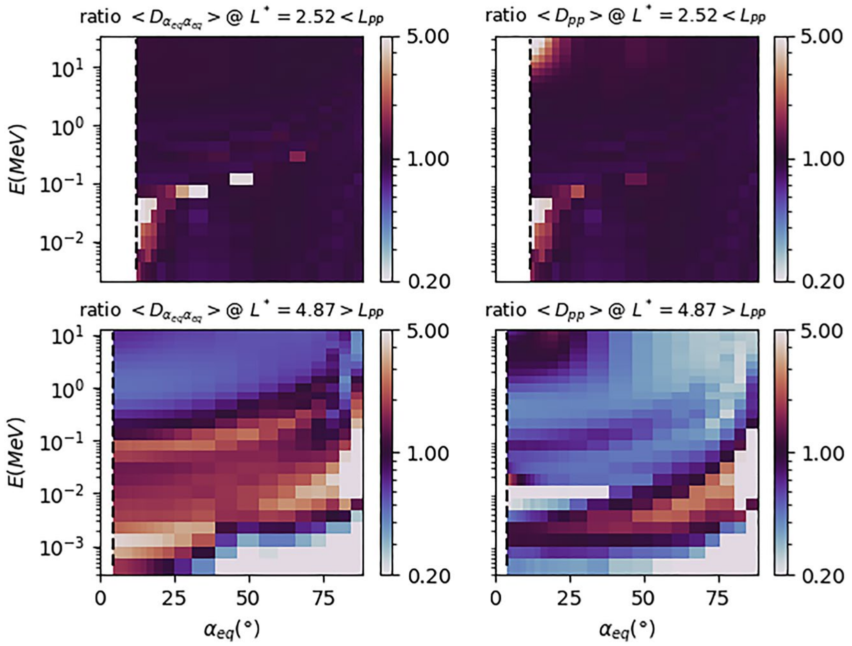

Figure 18. (α_{eq}, E) distribution of $\langle D_{\alpha_{eq}\alpha_{eq}} \rangle$, $\langle D_{pp} \rangle$ ratios in case of SPM density and Carpenter density, for two L^* on either sides of the plasmapause $(K_p = 2.3)$.

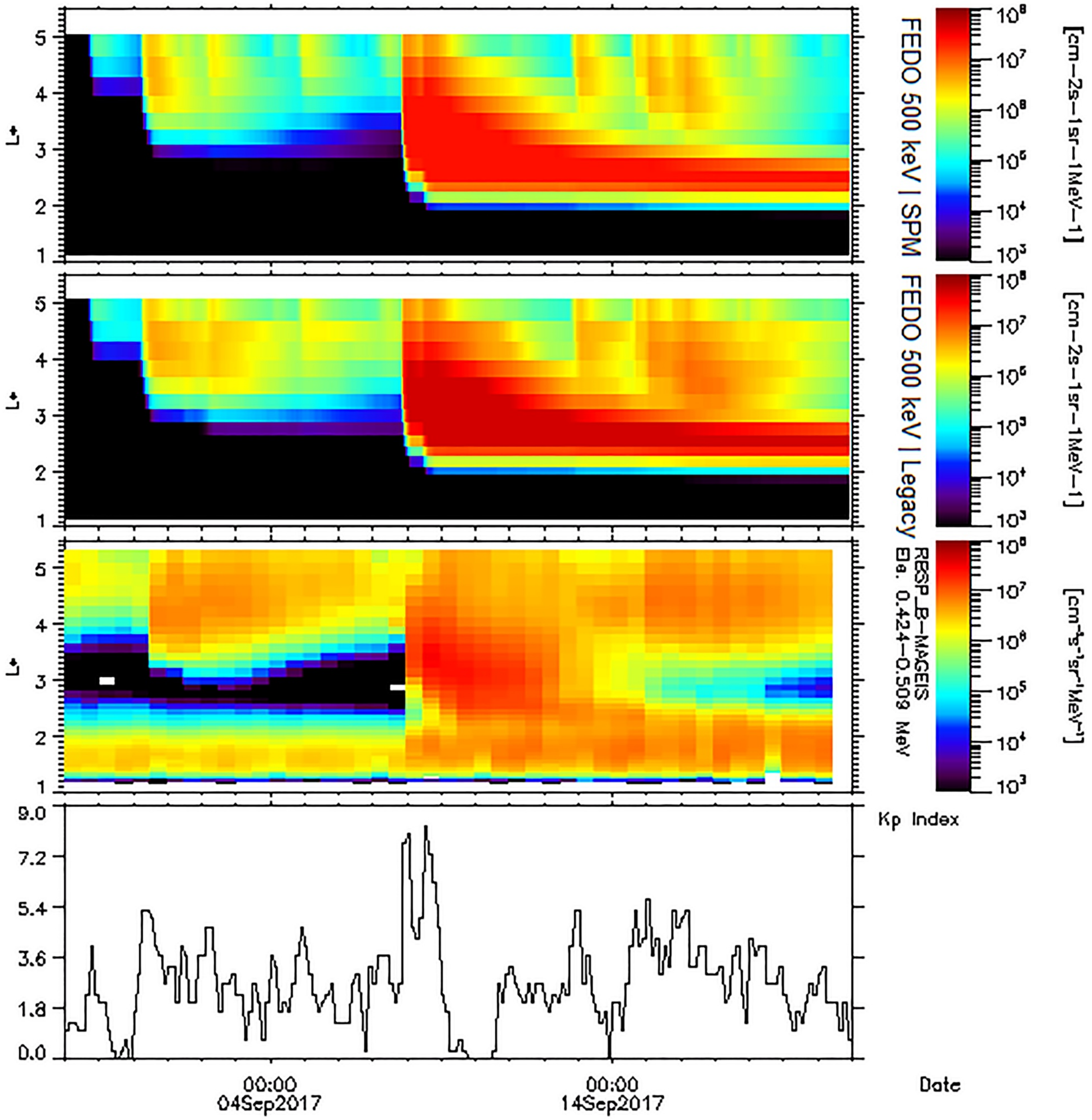

Figure 19. From the top to the bottom: Salammbô 500 keV electron flux results for the September 2017 event using the SPM time dependent density model, Salammbô 500 keV electron flux results using the Carpenter and Anderson density model, RBSP-B omnidirectional differential flux measurements for electrons at 0.424 – 0.509 MeV and Kp evolution during the studied event.

its computational efficiency by reducing the cost to generate one diffusion configuration to almost 1 minute. Besides, the method was validated against old WAPI results and proved its physical relevance with contained numerical errors. Finally, the new code FARWEST was put in use to measure the benefit of the SPM density model on Salammbô electron flux map estimation. This improvement should open the way to the establishment of radiation belt meta-codes, which would be capable to describe the inner magnetosphere medium and derive the dynamical frame they solve at each time iteration.

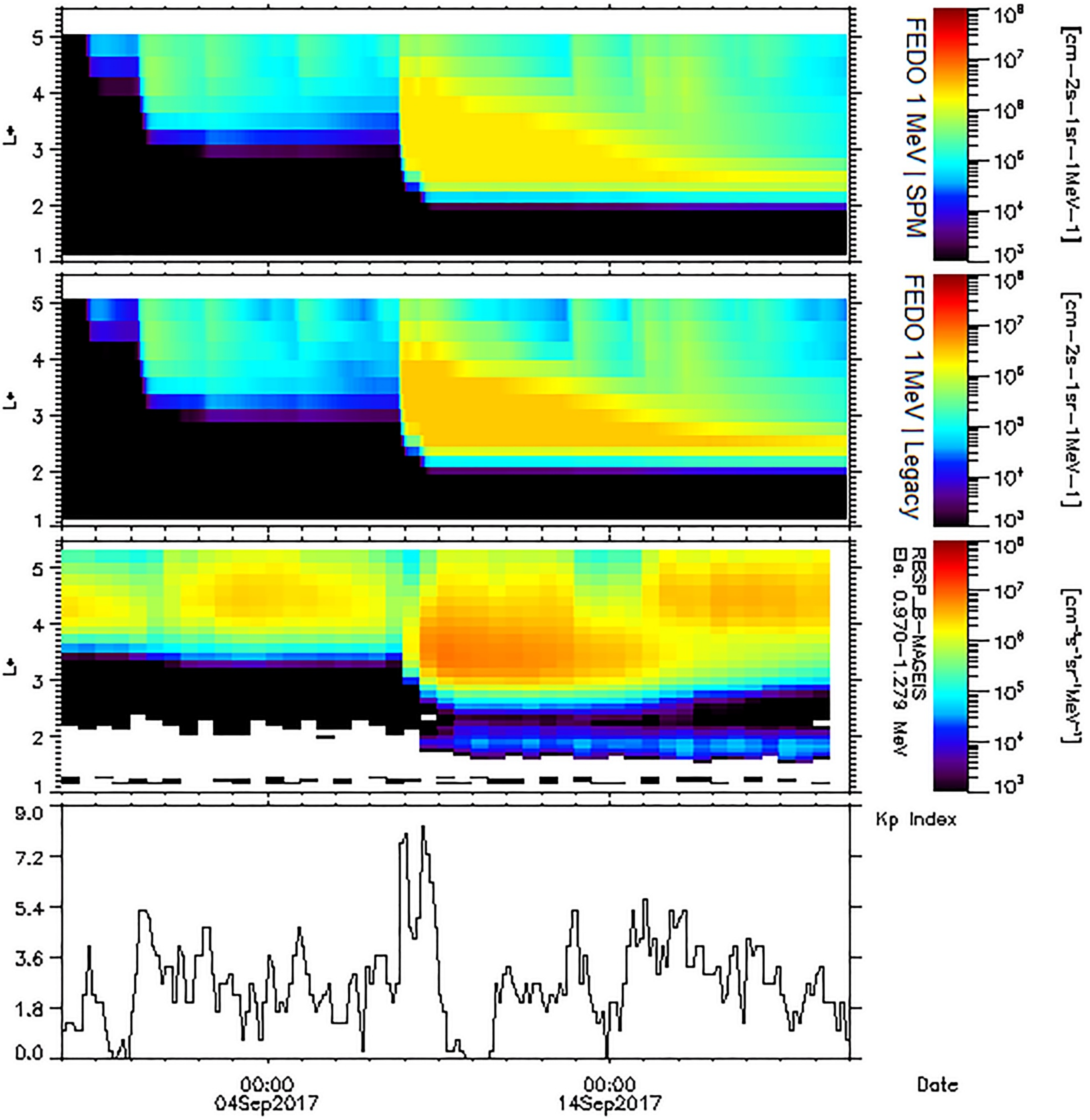

Figure 20. From the top to the bottom: Salammbô 1 MeV electron flux results for the September 2017 event using the SPM time dependent density model, Salammbô 1 MeV electron flux results using the Carpenter and Anderson density model, RBSP-B omnidirectional differential flux measurements for electrons at 0.970 – 1.279 MeV and Kp evolution during the studied event.

Appendix A

The normalization constant A^2 used in the Gaussian frequency distribution, is give, by

$$A^2 = \frac{B_\omega^2}{\partial\omega}\frac{2}{\sqrt{\pi}}\left[\mathrm{erf}\left(\frac{\omega_m - \omega_{lc}}{\partial\omega}\right) + \mathrm{erf}\left(\frac{\omega_{uc} - \omega_{lc}}{\partial\omega}\right)\right]^{-1} \tag{A1}$$

The expression of the local diffusion coefficients for a given harmonic n and a given angle $\psi = \tan^{-1} X$

$$D_{\alpha\alpha}^{nX} = \sum_i \frac{q_\sigma^2 \omega_i^2}{4\pi\left(1+X^2\right) N\left(\omega_i\right)} \left[\frac{n\Omega_\sigma/\gamma\omega_i - \sin^2\alpha}{\cos\alpha}\right]^2 B^2\left(\omega_i\right) g(X) \left.\frac{|\Phi_{n,k}|^2}{|v_\parallel - \frac{\partial\omega}{\partial k_\parallel}|}\right|_{k_{\parallel_i}} \tag{A2}$$

$$D_{pp}^{nX} = D_{\alpha\alpha}^{nX} \left[\frac{\sin\alpha\,\cos\alpha}{\frac{n\Omega_\sigma}{\gamma\omega_i} - \sin^2\alpha}\right]_{k_{\parallel_i}}^2 \tag{A3}$$

$$D_{\alpha p}^{nX} = D_{\alpha\alpha}^{nX} \left[\frac{\sin\alpha\,\cos\alpha}{\frac{n\Omega_\sigma}{\gamma\omega_i} - \sin^2\alpha}\right]_{k_{\parallel_i}} \tag{A4}$$

With $N(\omega)$ the normalization factor ensuring that the wave energy per unit frequency is given by $B^2(\omega)$

$$N(\omega) = \frac{1}{2\pi^2}\int_{X_{min}}^{X_{max}} \frac{g(X)k^2}{\left(1+X^2\right)^{\frac{3}{2}}} \frac{\partial D}{\partial\omega}\left[\frac{\partial D}{\partial k}\right]^{-1} XdX \tag{A5}$$

The term $|\Phi|_{k,n}^2$ depends on the Bessel function J_n and is given by

$$\begin{aligned}|\Phi|_{k,n}^2 = &\left[\left(\left(\frac{\mu - L}{\mu^2 - S}\right) J_{n+1} + \left(\frac{\mu^2 - R}{\mu^2 - S}\right) J_{n-1}\right)\left(\frac{\mu^2\sin^2\psi - P}{2\mu^2}\right) + \cot\alpha\sin\psi\,\cos\psi\,J_n\right]^2 \\ &\left[\left(\frac{R - L}{2\left(\mu^2 - S\right)}\right)^2\left(\frac{P - \mu^2\sin^2\psi}{\mu^2}\right)^2 + \left(\frac{P\,\cos\psi}{\mu^2}\right)^2\right]^{-1}\end{aligned} \tag{A6}$$

The bounce-averaged diffusion coefficients, for equatorial pitch-angle α_{eq} are given by

$$\left\langle D_{\alpha_{\mathrm{eq}}\alpha_{\mathrm{eq}}}\right\rangle = \frac{1}{\tau_B}\int_0^{\tau_b} D_{\alpha\alpha}\left(\frac{\partial\alpha_{\mathrm{eq}}}{\partial\alpha}\right)^2 \mathrm{dt} \tag{A7}$$

$$\left\langle D_{\alpha_{\mathrm{eq}}\alpha_{\mathrm{eq}}}\right\rangle = \frac{1}{\tau_B}\int_0^{\tau_b} D_{\alpha\alpha}\left(\frac{\partial\alpha_{\mathrm{eq}}}{\partial\alpha}\right) \mathrm{dt} \tag{A8}$$

$$\left\langle D_{pp}\right\rangle = \frac{1}{\tau_B}\int_0^{\tau_b} D_{pp}dt \tag{A9}$$

Where τ_b is the particle bounce period.

Data Availability Statement

The computing method followed in WAPI is based on the developments described in (Glauert & Horne, 2005). The cold plasma density model used in the validation procedure is taken from (Carpenter & Anderson, 1992) and the VLF intensities are taken from the (Meredith et al., 2012).

Acknowledgments

The SafeSpace project has received funding from the European Union's Horizon 2020 research and innovation program under grant agreement No 870437.

References

Abel, B., & Thorne, R. M. (1998). Electron scattering loss in earth's inner magnetosphere: 2. Sensitivity to model parameters. *Journal of Geophysical Research*, *103*(A2), 2397–2407. https://doi.org/10.1029/97JA02920

Albert, J. M. (1999). Analysis of quasi-linear diffusion coefficients. *Journal of Geophysical Research*, *104*(A2), 2429–2441. https://doi.org/10.1029/1998JA900113

Allison, H. J., Shprits, Y. Y., Zhelavskaya, I. S., Wang, D., & Smirnov, A. G. (2021). Gyroresonant wave-particle interactions with chorus waves during extreme depletions of plasma density in the van allen radiation belts. *Science Advances*, *7*(5), eabc0380. https://doi.org/10.1126/sciadv.abc0380

Baker, D. N., Blake, J. B., Callis, L. B., Cummings, J. R., Hovestadt, D., Kanekal, S., et al. (1994). Relativistic electron acceleration and decay time scales in the inner and outer radiation belts: Sampex. *Geophysical Research Letters*, *21*(6), 409–412. https://doi.org/10.1029/93GL03532

Baker, D. N., Blake, J. B., Klebesadel, R. W., & Higbie, P. R. (1986). Highly relativistic electrons in the Earth's outer magnetosphere: 1. Lifetimes and temporal history 1979–1984. *Journal of Geophysical Research*, *91*(A4), 4265. https://doi.org/10.1029/JA091iA04p04265

Beutier, T., & Boscher, D. (1995). A three-dimensional analysis of the electron radiation belt by the Salammbô code. *Journal of Geophysical Research*, *100*(A8), 14853. https://doi.org/10.1029/94JA03066

Boscher, D., Bourdarie, S., Maget, V., Sicard-Piet, A., Rolland, G., & Standarovski, D. (2018). High-energy electrons in the inner zone. *IEEE Transactions on Nuclear Science*, *65*(8), 1546–1552. https://doi.org/10.1109/TNS.2018.2824543

Carpenter, D. L., & Anderson, R. R. (1992). An ISEE/whistler model of equatorial electron density in the magnetosphere. *Journal of Geophysical Research*, *97*(A2), 1097. https://doi.org/10.1029/91JA01548

Daglis, I. A., Bourdarie, S., Rodriguez, J. C., Darrouzet, F., Benoit, L., Poedts, S., et al. (2021). Improving nowcasting and forecasting of the sun-to-belts space weather chain through the H2020 SafeSpace project. EGU21-13466. https://doi.org/10.5194/egusphere-egu21-13466

Dahmen, N., Rogier, F., & Maget, V. (2020). On the modelling of highly anisotropic diffusion for electron radiation belt dynamic codes. *Computer Physics Communications*, *254*, 107342. https://doi.org/10.1016/j.cpc.2020.107342

Glauert, S. A., & Horne, R. B. (2005). Calculation of pitch angle and energy diffusion coefficients with the PADIE code: Padie diffusion code. *Journal of Geophysical Research*, *110*(A4), A04206. https://doi.org/10.1029/2004JA010851

Glauert, S. A., Horne, R. B., & Meredith, N. P. (2014). Three-dimensional electron radiation belt simulations using the BAS radiation belt model with new diffusion models for chorus, plasmaspheric Hiss, and lightning-generated whistlers. *Journal of Geophysical Research: Space Physics*, *119*(1), 268–289. https://doi.org/10.1002/2013JA019281

Horne, R. B., Thorne, R. M., Glauert, S. A., Meredith, N. P., Pokhotelov, D., & Santolík, O. (2007). Electron acceleration in the van allen radiation belts by fast magnetosonic waves. *Geophysical Research Letters*, *34*(17), L17107. https://doi.org/10.1029/2007GL030267

Horne, R. B., Thorne, R. M., Shprits, Nigel P. Meredith, Sarah A. Glauert, Andy J. Smith, Shrikanth G. Kanekal, Daniel N. Baker, Mark J. Engebretson, Jennifer L. Posch, Y. Y., Spasojevic, M., Inan, U. S., Pickett, J. S., et al. (2005). Wave acceleration of electrons in the van allen radiation belts. *Nature*, *437*(7056), 227–230. https://doi.org/10.1038/nature03939

Hudson, M. K., Kress, B. T., Mueller, H.-R., Zastrow, J. A., & Bernard Blake, J. (2008). Relationship of the van allen radiation belts to solar wind drivers. *Journal of Atmospheric and Solar-Terrestrial Physics*, *70*(5), 708–729. https://doi.org/10.1016/j.jastp.2007.11.003

Kennel, C. F., & Engelmann, F. (1966). Velocity space diffusion from weak plasma turbulence in a magnetic field. *The Physics of Fluids*, *9*(12), 2377–2388. https://doi.org/10.1063/1.1761629

Kennel, C. F., & Petschek, H. E. (1966). Van allen belt plasma Physics.

Li, X., Baker, D. N., Temerin, M., Larson, D., Lin, R. P., Reeves, G. D., et al. (1997). Are energetic electrons in the solar wind the source of the outer radiation belt? *Geophysical Research Letters*, *24*(8), 923–926. https://doi.org/10.1029/97GL00543

Lyons, L. R. (1974a). Electron diffusion driven by magnetospheric electrostatic waves. *Journal of Geophysical Research*, *79*(4), 575–580. https://doi.org/10.1029/JA079i004p00575

Lyons, L. R. (1974b). Pitch angle and energy diffusion coefficients from resonant interactions with ion–cyclotron and whistler waves. *Journal of Plasma Physics*, *12*(3), 417–432. https://doi.org/10.1017/S002237780002537X

Lyons, L. R., & Thorne, R. M. (1973). Equilibrium structure of radiation belt electrons. *Journal of Geophysical Research*, *78*(13), 2142–2149. https://doi.org/10.1029/JA078i013p02142

Lyons, L. R., Thorne, R. M., & Kennel, C. F. (1972). 'Pitch-Angle diffusion of radiation belt electrons within the plasmasphere'. *Journal of Geophysical Research*, *77*(19), 3455–3474. https://doi.org/10.1029/JA077i019p03455

Meredith, N. P. (2003). Statistical analysis of relativistic electron energies for cyclotron resonance with EMIC waves observed on CRRES. *Journal of Geophysical Research*, *108*(A6), 1250. https://doi.org/10.1029/2002JA009700

Meredith, N. P., Horne, R. B., & Anderson, R. R. (2008). Survey of magnetosonic waves and proton ring distributions in the Earth's inner magnetosphere: Magnetosonic waves. *Journal of Geophysical Research*, *113*(A6), A06213. https://doi.org/10.1029/2007JA012975

Meredith, N. P., Horne, R. B., Sicard-Piet, A., Boscher, D., Yearby, K. H., Wen, L., & Thorne, R. M. (2012). Global model of lower band and upper band Chorus from multiple satellite observations: Global model of whistler mode chorus. *Journal of Geophysical Research*, *117*(A10), A10225. https://doi.org/10.1029/2012JA017978

Ni, B., Thorne, R. M., Shprits, Y. Y., & Jacob, B. (2008). Resonant scattering of plasma sheet electrons by whistler-mode chorus: Contribution to diffuse auroral precipitation. *Geophysical Research Letters*, *35*(11), L11106. https://doi.org/10.1029/2008GL034032

Orlova, K. G., & Shprits, Y. Y. (2011). On the bounce-averaging of scattering rates and the calculation of bounce period. *Physics of Plasmas*, *18*(9), 092904. https://doi.org/10.1063/1.3638137

Pierrard, V., Botek, E., & Darrouzet, F. (2021). Improving predictions of the 3D dynamic model of the plasmasphere. *Frontiers in Astronomy and Space Sciences*, *8*, 681401. https://doi.org/10.3389/fspas.2021.681401

Pierrard, V., & Stegen, K. (2008). A three-dimensional dynamic kinetic model of the plasmasphere: 3-D dynamic kinetic plasmasphere. *Journal of Geophysical Research*, *113*(A10), A10209. https://doi.org/10.1029/2008JA013060

Pierrard, V., & Voiculescu, M. (2011). The 3D model of the plasmasphere coupled to the ionosphere: Plasmasphere coupled to the ionosphere. *Geophysical Research Letters*, *38*(12), L12104. https://doi.org/10.1029/2011GL047767

Santolík, O., Miyoshi, Y., Kolmašová, I., Matsuda, S., Hospodarsky, G. B., Hartley, D. P., et al. (2021). Inter-calibrated measurements of intense whistlers by arase and van allen probes. *Journal of Geophysical Research: Space Physics*, *126*(9), e2021JA029700. https://doi.org/10.1029/2021JA029700

Schulz, M., & Lanzerotti, L. J. (1974). Pitch-Angle diffusion. In M. Schulz & L. J. Lanzerotti (Eds.), *Particle diffusion in the radiation belts* (pp. 46–80). Springer.

Shprits, Y. Y., Subbotin, D., & Ni, B. (2009). Evolution of electron fluxes in the outer radiation belt computed with the VERB code: Verb code. *Journal of Geophysical Research*, *114*(A11), A11209. https://doi.org/10.1029/2008JA013784

Sicard-Piet, A., Boscher, D., Horne, R. B., Meredith, N. P., & Maget, V. (2014). Effect of plasma density on diffusion rates due to wave particle interactions with Chorus and plasmaspheric Hiss: Extreme event analysis. *Annales Geophysicae*, *32*(8), 1059–1071. https://doi.org/10.5194/angeo-32-1059-2014

Sicard-Piet, A., Bourdarie, S., & Boscher, D. (2008). WAPI: A new model for the WAve particle interaction. *37*, 2890.

Stix, T. H. (1962). The theory of plasma waves.

Su, Z., Xiao, F., Zheng, H., & Wang, S. (2010). STEERB: A three-dimensional code for storm-time evolution of electron radiation belt: Steerb code. *Journal of Geophysical Research*, *115*(A9), A09208. https://doi.org/10.1029/2009JA015210

Su, Z., Xiao, F., Zheng, H., & Wang, S. (2011). Radiation belt electron dynamics driven by adiabatic transport, radial diffusion, and wave-particle interactions: Influence of adiabatic transport. *Journal of Geophysical Research*, *116*(A4), A04205. https://doi.org/10.1029/2010JA016228

Subbotin, D. A., & Shprits, Y. Y. (2009). Three-Dimensional modeling of the radiation belts using the versatile electron radiation belt (verb) code: Modeling of the radiation belts. *Space Weather*, *7*(10), S100001. https://doi.org/10.1029/2008SW000452

Summers, D. (2003). Relativistic electron pitch-angle scattering by electromagnetic ion cyclotron waves during geomagnetic storms. *Journal of Geophysical Research*, *108*(A4), 1143. https://doi.org/10.1029/2002JA009489

Thorne, R. M. (2010). Radiation belt dynamics: The importance of wave-particle interactions: Frontier. *Geophysical Research Letters*, *37*(22), L22107. https://doi.org/10.1029/2010GL044990

Thorne, R. M., O'Brien, T. P., Shprits, Y. Y., Summers, D., & Horne, R. B. (2005). Timescale for MeV electron microburst loss during geomagnetic storms: Timescale for microburst loss. *Journal of Geophysical Research*, *110*(A9), A09202. https://doi.org/10.1029/2004JA010882

Tsurutani, B. T., & Smith, E. J. (1974). Postmidnight Chorus: A substorm phenomenon. *Journal of Geophysical Research*, *79*(1), 118–127. https://doi.org/10.1029/JA079i001p00118

Usanova, M. E., Darrouzet, F., Mann, I. R., & Bortnik, J. (2013). Statistical analysis of EMIC waves in plasmaspheric plumes from cluster observations: Emic waves in plasmaspheric plumes. *Journal of Geophysical Research: Space Physics*, *118*(8), 4946–4951. https://doi.org/10.1002/jgra.50464

Varotsou, A., Boscher, D., Bourdarie, S., Horne, R. B., Glauert, S. A., & Meredith, N. P. (2005). Simulation of the outer radiation belt electrons near geosynchronous orbit including both radial diffusion and resonant interaction with whistler-mode Chorus waves: Outer electron radiation belt simulation. *Geophysical Research Letters*, *32*(19), L19106. https://doi.org/10.1029/2005GL023282